Nanoscale Horizons

ROYAL SOCIETY OF CHEMISTRY

COMMUNICATION

View Article Online
View Journal | View Issue

Cite this: *Nanoscale Horiz.*, 2024, 9, 2273

Received 10th April 2024,
Accepted 16th September 2024

DOI: 10.1039/d4nh00159a

rsc.li/nanoscale-horizons

In situ studies revealing the effects of Au surfactant on the formation of ultra-thin Ag layers using high-power impulse magnetron sputter deposition†

Suzhe Liang, ‡§[a] Tianfu Guan,‡[a] Shanshan Yin,¶[a] Suo Tu,[a] Renjun Guo,[a] Yusuf Bulut, [ab] Kristian A. Reck, [c] Jonas Drewes,[c] Wei Chen, [d] Thomas Strunskus, [c] Matthias Schwartzkopf, [b] Franz Faupel, [c] Stephan V. Roth, [be] Ya-Jun Cheng [fg] and Peter Müller-Buschbaum *[a]

Introducing metallic nanoparticles, such as Au, on a substrate as a surfactant or wetting inducer has been demonstrated as a simple but effective way to facilitate the formation of ultra-thin silver layers (UTSLs) during the subsequent Ag deposition. However, most studies have paid much attention to the applications of UTSLs assisted by metallic surfactants but neglected the underlying mechanisms of how the metallic surfactant affects the formation of UTSL. Herein, we have applied *in situ* grazing-incidence wide-/small-angle X-ray scattering to reveal the effects of the Au surfactant or seed layer (pre-deposited Au nanoparticles) on the formation of UTSL by high-power impulse magnetron sputter deposition (HiPIMS) on a zinc oxide (ZnO) thin film. The comprehensive and in-depth analysis of the *in situ* X-ray scattering data revealed that the pre-deposited Au nanoparticles can act as additional defects or growth cores for the sputtered Ag atoms despite using HiPIMS, which itself forms many nucleation sites. As a result, the formation of a continuous and smooth UTSL is reached earlier in HiPIMS compared with bare ZnO thin films. Based on the mechanism revealed by the *in situ* measurements, we provide insight into the formation of UTSL and further UTSL-based applications.

New concepts

Ultra-thin silver layers (UTSLs) are regarded among the most promising candidates for achieving transparent conductive electrodes (TCEs) for various flexible and wearable electronic devices. It is critical to realize continuous UTSLs with minimized thickness. During the deposition of the silver (Ag) layer, the introduction of metallic nanoparticles as the surfactant has been demonstrated as an effective way to prepare the UTSL with continuous surface morphology with less Ag loading. In this work, we reveal the underlying mechanism of how the gold (Au) surfactant affects the formation of the subsequent UTSL growth deposited by high-power impulse magnetron sputter deposition (HiPIMS). We applied *in situ* grazing-incidence X-ray wide-/small-angle scattering (GIWAXS/GISAXS) during the Ag deposition to investigate the crystalline structure and morphology (size and inter-distance of Ag clusters) evolutions of the Ag layer, respectively. Based on a comprehensive analysis, we concluded that the pre-deposited Au surfactant could act as nuclei or growth cores for sputtered Ag atoms, leading to the formation of large and fixed Ag clusters and finally, continuous and smooth UTSL formation *via* the HiPIMS process.

[a] *Technical University of Munich, TUM School of Natural Sciences, Department of Physics, Chair for Functional Materials, James-Franck-Str. 1, 85748 Garching, Germany. E-mail: muellerb@ph.tum.de*
[b] *Deutsches Elektronen-Synchrotron DESY, Notkestr. 85, 22607 Hamburg, Germany*
[c] *Lehrstuhl für Materialverbunde, Institut für Materialwissenschaft, Christian-Albrechts-Universität zu Kiel, Kaiserstr. 2, 24143 Kiel, Germany*
[d] *Shenzhen Key Laboratory of Ultraintense Laser and Advanced Material Technology, Center for Advanced Material Diagnostic Technology, and College of Engineering Physics, Shenzhen Technology University, Lantian Road 3002, Pingshan, Shenzhen 518118, P. R. China*
[e] *KTH Royal Institute of Technology, Department of Fibre and Polymer Technology, Teknikringen 56-58, SE-100 44 Stockholm, Sweden*
[f] *Ningbo Institute of Materials Technology & Engineering, Chinese Academy of Sciences, 1219 Zhongguan West Rd, Zhenhai District, Ningbo, Zhejiang Province, 315201, P. R. China*
[g] *College of Renewable Energy, Hohai University, 1915 Hohai Avenue, Changzhou, Jiangsu Province 213200, P. R. China*

† Electronic supplementary information (ESI) available: Cross-sectional SEM images, AFM images, UV-vis reflectance spectra, IV-curves, photographs of sputter chamber and *in situ* GISAXS/GIWAXS setup, 2D GIWAXS patterns, 2D GISAXS patterns, and illustration of geometrical model for the GISAXS data analysis. See DOI: https://doi.org/10.1039/d4nh00159a

‡ S. Liang and T. Guan contribute equally to this work.

§ Present address: Eastern Institute for Advanced Study, Eastern Institute of Technology, Ningbo 315201, P. R. China.

¶ Present address: School of Mathematics and Physics, Jiangsu University of Technology, Changzhou 213001, P. R. China.

Introduction

The development of optoelectronic devices in recent years, including various sensors, thin-film solar cells, portable energy harvesters, and light-emitting diodes (LEDs), has profoundly affected and changed our daily lives.[1–6] As an essential component of advanced optoelectronic devices, transparent conductive electrodes (TCEs) with high electrical conductivity and optical transparency functionally ensure the transport of electrons and photons within the devices.[7–9] Indium tin oxide (ITO) is currently one of the most widely used TCEs and it provides a relatively high transmittance of over 80% in the visible spectral range and a low sheet resistance of about 10 Ω sq^{-1}, with a thickness of 100–200 nm.[10] However, large-scale application introduces several challenges to ITO electrodes. On the one hand, the increasing price of the raw material (indium) and inevitable material waste during production lead to serious cost concerns for ITO electrodes.[11,12] On the other hand, portability, flexibility, and wearability have been the most important requirements of optoelectronic devices for applications in different complex conditions.[13] The risk of microscopic crack formation because of the intrinsic brittleness of ITO hinders its application in flexible optoelectronic devices.[14] Therefore, it is necessary to develop desirable alternative TCEs to replace ITO electrodes, meeting the requirements of advanced flexible optoelectronic devices. Among the different attempts to realize novel TCEs, ultra-thin metal layers (UTMLs) have been considered as one of the most promising candidates owing to their excellent conductivity, optical transparency within the visible wavelength region, high flexibility, and sufficient mechanical stability.[15,16]

Achieving continuous UTMLs with both reasonable electrical conductivity and optical transparency is always a challenge to developing high-performance TCEs for flexible electronic devices. Conventional physical deposition techniques, including sputter deposition and evaporation, are the most widely used methods to prepare metal layers on different substrates.[17,18] However, in the case of thermal deposition processes, a metal layer typically follows a 3D (Volmer–Weber) growth mode, where discrete clusters or islands are formed initially, leading to the formation of a non-continuous morphology within a limited thickness and poor conductivity.[19,20] The formation of a continuous metal layer can be realized by increasing the metal film thickness or deposition rate[21] but this results in a dramatic reduction in the optical transmittance. To transform the 3D growth into a 2D growth mode of the deposited metal layers and form a continuous morphology within a limited thickness, several strategies have been proposed and effective results were obtained.[15,16] Generally, the main idea for fabricating UTMLs is to improve the wetting of target metal clusters by reducing the surface free energy of the metal clusters and the interfacial free energy between the metal clusters and the substrate. The reduction of surface and interfacial energies leads to the formation of more thermodynamically stable metal clusters and therefore an improvement in metal wetting.[22,23] Presently, the developed strategies for UTML fabrications are primarily around modifications of the target metals, deposition substrates, and deposition conditions to optimize metal wetting at a minimized thickness, including a second metal or gas as additions to the target metal,[24,25] the introduction of oxide supports,[26] metallic and non-metallic surfactants,[27,28] and the reduction of the deposition temperature.[29] Among these strategies, using metallic surfactants as wetting inducers has been demonstrated as very effective for fabricating UTMLs within a thickness of a few nanometers.[30,31]

Silver (Ag) is always a very promising electrode candidate for various electronic devices due to its high conductivity, high optical transparency in the visible region among metals, and relatively low costs.[32–34] In recent years, there have been various reports on efforts to prepare ultra-thin Ag layers (UTSLs) assisted by metallic surfactants or seed layers, such as gold (Au), aluminum (Al), copper (Cu), and germanium (Ge).[27,35–39] For example, Schwab *et al.* prepared UTSLs by using a 2-nm-thick Au wetting layer on a polymer substrate as the TCE of organic LEDs (OLEDs).[35] In their work, an almost closed homogeneous 5-nm-thick Ag layer was formed with the assistance of the Au wetting layer underneath, whereas the pure Ag layer without the Au wetting layer consisted of isolated grains at the same Ag thickness. Compared to the non-wetted Ag layer (5-nm-thick), the Au-wetted Ag layer exhibited a much lower sheet resistance and comparable transmittance. Moreover, continuous UTSLs can minimize the localized surface plasmon absorption effect. Xu *et al.* fabricated an 8-nm-thick calcium (Ca)-doped Ag layer assisted by an Al seed layer on a molybdenum(VI) oxide (MoO_3) substrate, which also acted as a TCE for flexible OLEDs.[40] With the Al seed layer, the prepared ultra-thin Ag/Ca layer also exhibited a smoother surface morphology and a lower sheet resistance. Jeong *et al.* studied how the Ge seed layer affected the wettability and growth of UTSL on a zinc oxide (ZnO) substrate.[37] It was suggested that the Ge seed layer could reduce the thermodynamic free energy at both the top and bottom boundaries of evolving Ag regions. As discussed above, introducing metallic surfactants as wetting or seed layers has been demonstrated as an effective method to fabricate UTSLs with competitive electrical and optical performances. However, only a few studies have focused on the underlying mechanisms of how metallic surfactants affect the growth of UTSLs. Moreover, from the existing studies, which are mainly based on *ex situ* experiments, it is hard to completely understand the effects of metallic surfactants on UTSL growth. Therefore, we have applied *in situ* characterization techniques to probe the effects of metallic surfactants on the formation of UTSLs in real time.

Grazing-incidence wide-/small-angle X-ray scattering (GIWAXS/GISAXS) are among the most powerful techniques for investigating the crystal structures and nanostructures of various thin-film configurations.[41–43] It is possible to monitor structural evolutions during the formation of thin films and the operation of thin film-based devices in real time.[44–46] Previously, we successfully applied *in situ* GISAXS to study the growth kinetics of ultra-thin Au layers on different substrates.[47–49] Based on an advanced analysis model, we extracted detailed dimensional information on sputter-deposited Au clusters and determined

key points of the Au growth during a four-stage model, mainly based on the Volmer–Weber mode.

In this work, we focus on the formation of sputter-deposited UTSLs on a ZnO support with the assistance of an Au surfactant. The UTSLs were prepared with high-power impulse magnetron sputter deposition (HiPIMS), a technique that forms more nucleation sites for metal cluster growth compared with other sputter deposition methods. Thus, compared with conventional direct current magnetron sputtering (DCMS) for metal layer deposition, HiPIMS can increase the adhesion between the deposited metal film and the substrate.[50–52] Recently, Reck *et al.* compared in detail the effects of HiPIMS, bipolar HiPIMS, and DCMS on the growth behavior of the Ag layer on SiO_2 and polystyrene substrates, respectively.[53] The effects of the Au surfactant on the growth kinetics of UTSLs were investigated in-depth by using *in situ* GIWAXS and GISAXS. The GIWAXS data provided the crystalline information of formed Ag clusters during the sputter deposition process, while the GISAXS data revealed the morphology evolution of sputter-deposited Ag clusters. With further analysis of the *in situ* GISAXS data, the mechanism was proposed for how the Au surfactant facilitates the formation of UTSLs on the ZnO support. The use of Au as a surfactant for the formation of UTSL is not a new method but our focus in this work is on how the pre-deposited Au surfactant affects the growth behavior of further-deposited UTSL. By using *in situ* GIWAXS/GISAXS to investigate the structural (crystalline structure) and morphological (size and inter-distance) evolutions of the UTSL during sputtering with and without the presence of Au surfactant, we sought a deeper understanding of the UTSL formation. This understanding is expected to provide a foundation for future work on optimizing UTSL fabrication methods and tuning the nanostructure of UTSLs for various applications.

Experimental section

Materials

Zinc acetate dehydrate (99.9%), 2-methoxyethanol (99.8%) and monoethanolamine (99.5%) were purchased from Sigma-Aldrich. Hydrogen peroxide (H_2O_2, 30%), sulfuric acid (H_2SO_4, 98%), and concentrated hydrochloric acid (HCl, 37%) were purchased from Carl Roth GmbH & Co. KG. Silicon wafers (Si 100, p-type) were purchased from Silchem Handels GmbH (Freiberg, Germany). Gold (99.99%) for evaporation was purchased from Goldkontor GmbH (Hamburg, Germany). Silver (99.999%) for sputtering was purchased from Kurt J. Lesker (United States). All chemicals were used as-received without further purification.

Preparation of ZnO and ZnO/Au substrates

ZnO sol (0.2 M) was prepared by dissolving zinc acetate dehydrate in a mixed solution of 2-methoxy ethanol and monoethanolamine (the molar ratio of monoethanolamine to zinc acetate was kept at 1 : 1) under continuous stirring at 60 °C for 2 h.[54] ZnO thin films were spin-coated on cleaned Si substrates at 3000 rpm for 30 s, followed by an annealing process on a hot plate at 250 °C for 30 min. The Si substrates (*ca.* 15 mm × 12 mm) were cleaned in an acid bath comprising 54 mL deionized water, 84 mL H_2O_2, and 198 mL H_2SO_4 for 20 min at 80 °C. For ZnO/Au substrates, Au surfactant was evaporated on the as-prepared ZnO thin films up to a thickness of 2 nm (0.2 Å s^{-1}) under a vacuum of 10^{-2} mbar. Here, we chose polished Si wafers, which have very smooth surfaces, as the substrates for preparing ZnO and ZnO/Au thin films to ensure good sample alignment before measurement and good signal acquisition during the *in situ* GIWAXS/GISAXS measurements.

Preparation of UTSLs by sputter deposition

The sputter deposition of UTSLs on ZnO and ZnO/Au substrates was realized by a HiPIMS system. The details of the self-built sputter deposition chamber can be found in our previous article.[21] The sputter chamber was maintained under vacuum conditions with a pressure of 0.36 Pa by using a vacuum pump during all sputtering processes. Argon (Ar) was introduced into the chamber controlled by a mass flow to create an Ar plasma and trigger the sputter deposition. Therefore, the vacuum conditions are a dynamic equilibrium between vacuumizing and introducing Ar. The sputter parameters included a pulse length of 20 μs with a frequency of 150 Hz, the average power P = 40 W, the voltage U = (952 ± 4) V, and the peak current I = (1.41 ± 0.13) A cm^{-2}. The deposition rate J was determined by a quartz crystal microbalance (QCM) of (0.312 ± 0.006) nm s^{-1}. The deposition times were set at 5 s, 10 s, 20 s, and 30 s, corresponding to the effective thicknesses of about 1.6 nm, 3.1 nm, 6.4 nm, and 9.4 nm. For the non-heated samples, the sputter depositions were done at ambient temperature. Regarding the samples prepared at 100 °C, the sputter depositions were performed after the sample was heated (a heating module was mounted in the sample stage) to 100 °C.

In situ GIWAXS/GISAXS measurements

The HiPIMS system was mounted on the P03/MiNaXS beamline of the PETRA III storage ring at Deutsches Elektronen-Synchrotron (DESY, Hamburg, Germany) to integrate with the *in situ* GIWAXS/GISAXS setups.[55] The photon energy of the incidence X-ray was 11.72 keV, corresponding to the wavelength of 1.058 Å. The incident angle (α_i) was set as 0.4°. The sample-to-detector distance (SDD) was set to 193.5 mm for GIWAXS and 3230 mm for GISAXS. 2D GIWAXS and GISAXS data were collected by LAMBDA 9M (X-Spectrum, pixel size 55 μm, 2 images per second) and Pilatus 2M (Dectris, pixel size 172 μm, 20 images per second) detectors, respectively. To avoid possible X-ray radiation damage on the sample, the sample was repeatedly moved along the horizontal direction during the *in situ* GIWAXS/GISAXS measurements and checked for beam damage with scans along the sample plane. The on-site photographs of the HiPIMS system and the whole experimental setup for *in situ* GIWAXS and GISAXS measurements can be found in the ESI.†

FESEM, AFM, UV-vis, and sheet resistance measurements

The field-emission scanning electron microscopy (FESEM) images were obtained by a high-resolution FESEM (Zeiss

Gemini NVision 40, Germany) at a working distance of 3.5 mm and an accelerating voltage of 5 kV. The atomic force microscopy (AFM) images were obtained by a Nanosurf CoreAFM system (Switzerland) with a tapping mode and processed by Gwyddion.[56] The ultraviolet-visible (UV-vis) spectra were measured by a Lambda 35 instrument (PerkinElmer, United States) in normal-incidence reflectance mode with a wavelength range of 300–800 nm. The scanning speed was set to 240 nm min^{-1} with a step size of 1 nm. To determine the sheet resistances in UTSL/ZnO (δ_{Ag} = 9.4 nm) and UTSL/Au/ZnO (δ_{Ag} = 9.4 nm) thin films, four-point probe measurements were conducted using a Cascade Microtech (C4S-54/5) setup. The setup consisted of four equidistant tungsten carbide tips, with a spacing of 1 mm and tip radii of 125 μm. The tips were mounted on a spring to prevent piercing of the films. During the measurements, a current I was applied to the outer two tips, while the inner two tips measured the induced voltage U.

Results and discussion

We prepared ZnO thin films as the support for the growth of UTSLs since ZnO has been widely used as supporting or functional layers for metal electrodes in various electronic devices.[57–59] Compared to other oxides, ZnO is an ideal support for the formation of UTSL because Ag atoms could more easily form strong bonds with Ag–O bonds due to the weak Zn–O bonding.[60] As shown in Fig. 1(a), the ZnO supports are fabricated by spin-coating a ZnO sol on cleaned silicon (Si) substrates. The details about the preparation of the ZnO sol can be found in the Experimental section. The as-prepared ZnO support exhibited an irregular and rough surface morphology, as shown by the FESEM images in Fig. 1(c). As illustrated in Fig. 1(b), in the first step Au nanoparticles were evaporated on the ZnO support, acting as the surfactant or seed layer for the UTSL formation with an effective thickness (δ_{Au}) of 2 nm. Here, the choice of δ_{Au} = 2 nm for the pre-deposited Au surfactant layer was based on balancing having sufficient space between pre-deposited Au nanoparticles and minimizing the effect of pre-deposited Au nanoparticles on the further growth of Ag from the already existing metal loading.

As presented in Fig. 1(d), evaporated Au nanoparticles (bright tiny dots) were homogeneously distributed on the surface of the ZnO support with a diameter of 4.0 ± 0.2 nm. The thickness of the ZnO support was determined as 13.0 ± 0.9 nm by cross-section FESEM image analysis as shown in Fig. S1(a)

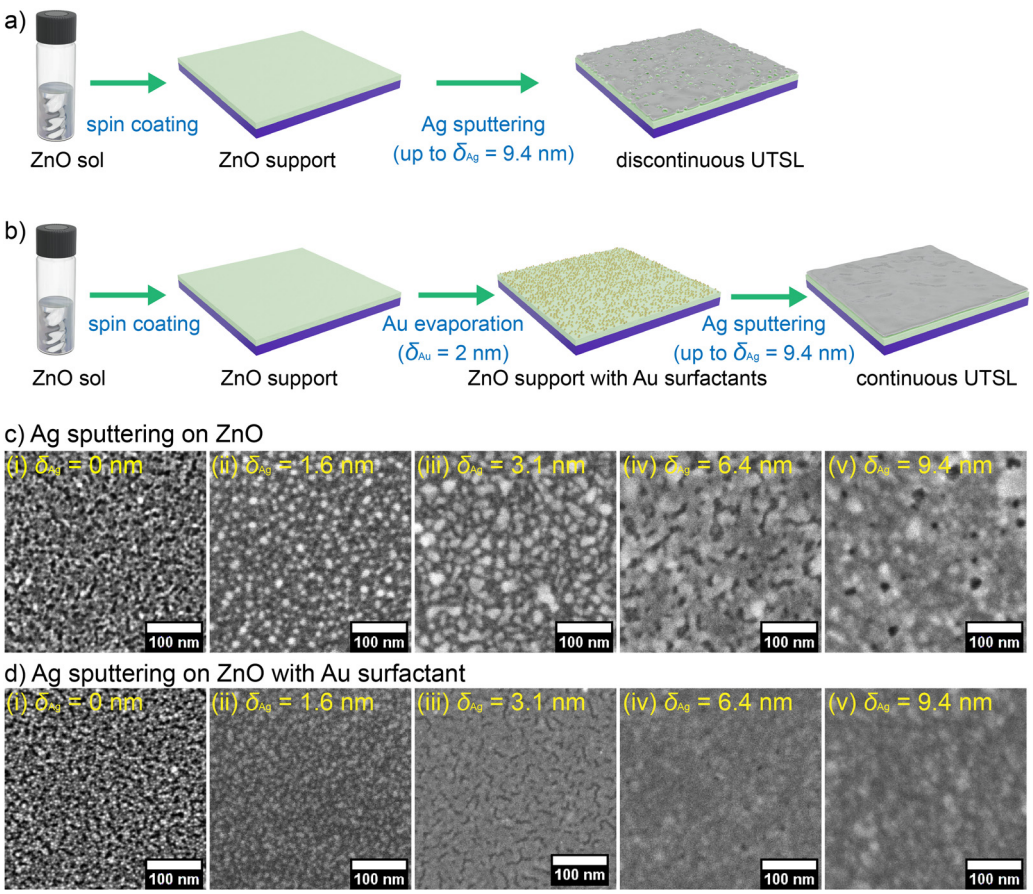

Fig. 1 Schematic showing the preparation processes of HiPIMS sputter-deposited UTSLs (a) on the bare ZnO support and (b) the ZnO support with pre-deposited Au surfactant or seed layer. FESEM images of sputter-deposited UTSLs on (c) the bare ZnO support and (d) the ZnO support with Au surfactant at different thicknesses of the UTSL δ_{Ag} = 0, 1.6, 3.1, 6.4, and 9.4 nm, respectively.

(ESI†). After the evaporation of the Au surfactant, the total thickness of the ZnO support and the Au layer slightly increased to 14.3 ± 0.8 nm, as shown in Fig. S1(b) (ESI†). In the second step, the UTSLs were deposited on ZnO supports without and with Au surfactant *via* HiPIMS up to the effective Ag thickness (δ_{Ag}) of 9.4 nm. At first glance, the growth processes of the UTSLs were revealed by FESEM at different effective Ag thicknesses, as presented in Fig. 1(b) and (c). At δ_{Ag} = 3.1 nm, the deposited Ag layer remains in discrete clusters on the bare ZnO support (Fig. 1(c-iii)), whereas a mainly continuous Ag layer was already formed on the ZnO support with Au surfactant (Fig. 1(d-iii)). On increasing the effective Ag thickness to 9.4 nm, the deposited Ag layer still did not form a completely continuous morphology, as shown in Fig. 1(c-v). From the cross-sectional view (at effective deposited thickness δ_{Ag} = 9.4 nm), the average thickness of the total layer without Au surfactant (Ag/ZnO) was 33.0 ± 3.6 nm, which is thicker than 25.4 ± 3.2 nm in the case with Au acting as the surfactant (Ag/Au/ZnO), as shown in Fig. S1(c) and (d) (ESI†). On subtracting the thickness of bare ZnO or Au/ZnO thin film from the total thickness after the HiPIMS deposition with δ_{Ag} = 9.4 nm, the real average thickness of the deposited Ag layer on Au/ZnO was about 11.1 nm, while the counterpart on the bare ZnO was about 20 nm. The calculated real average thickness of the deposited Ag layer on Au/ZnO (11.1 nm) was closer to the effective thickness of 9.4 nm after the sputter deposition, indicating that the deposited Ag layer on Au/ZnO was more homogeneous. It should be noted that in this work, all descriptions related to the thickness of the deposited Ag layer refer to the effective thickness instead of the real average thickness. We also measured the roughness of deposited UTSLs by AFM, as shown in Fig. S2 (ESI†). For the bare ZnO thin film, the root mean square roughness (R_{rms}) was measured as 0.38 ± 0.06 nm. After Ag sputter deposition, the R_{rms} increased to 5.2 ± 1.5 nm at δ_{Ag} = 3.1 nm and then further increased to 7.5 ± 1.4 nm at δ_{Ag} = 9.4 nm. In contrast, the R_{rms} of Au/ZnO thin film was 0.62 ± 0.07 nm, which is higher than that of the bare ZnO thin film, due to the existence of pre-deposited Au nanoparticles. After the subsequent Ag deposition, the R_{rms} also increased to 3.3 ± 0.8 nm at δ_{Ag} = 3.1 nm and 7.2 ± 1.8 nm at δ_{Ag} = 9.4 nm. This indicates that the existence of pre-deposited Au surfactant can lower the roughness of the deposited Ag layer, especially at low effective thickness. With increasing the Ag loading by sputtering, such effect was reduced, resulting in the comparable R_{rms} of the deposited Ag layers with and without Au surfactant at δ_{Ag} = 9.4 nm. The increased effective thickness of the whole metallic layer due to the presence of the pre-deposited Au nanoparticles also contributed to the reduction of roughness.

The optical responses of these UTSL/ZnO and UTSL/Au/ZnO thin films were measured using UV-vis reflectance spectra, as shown in Fig. S3 (ESI†). With the increase in of the effective Ag thickness δ_{Ag}, the reflectance within the visible range (400–800 nm) of both the UTSL/ZnO and UTSL/Au/ZnO thin films also increased due to the accumulation of sputter-deposited Ag. Compared with the UTSL/ZnO thin films, the reflectance of UTSL/Au/ZnO thin films was higher because of the more compact morphology of the deposited Ag layers.[61] The conductivities (σ) of UTSL/ZnO (δ_{Ag} = 9.4 nm) and UTSL/Au/ZnO (δ_{Ag} = 9.4 nm) thin films were determined by sheet resistance measurements, as shown in Fig. S4 (ESI†). As a result, the σ value of UTSL/Au/ZnO (δ_{Ag} = 9.4 nm) thin films was calculated as (9.3 ± 2.6) × 10^5 S cm^{-1}, which is higher than that of (4.5 ± 1.0) × 10^5 S cm^{-1} of UTSL/ZnO (δ_{Ag} = 9.4 nm) thin films. The increased conductivity of UTSL/Au/ZnO (δ_{Ag} = 9.4 nm) thin films is attributed to its more continuous Ag film morphology.

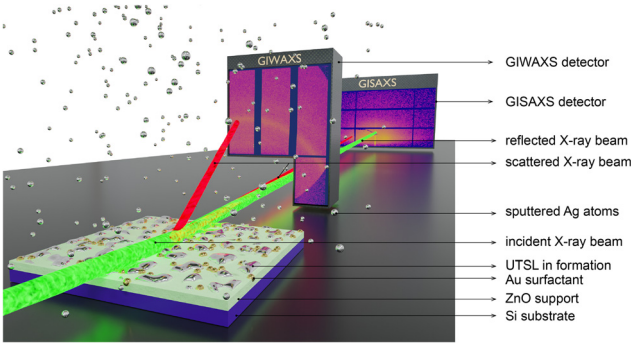

Fig. 2 Schematic of the formation of ULSL by HiPIMS Ag sputter deposition on the ZnO support with Au surfactant (pre-deposited Au nanoparticles), investigated *via in situ* GIWAXS and GISAXS measurements.

To investigate the effect of the Au surfactant on the formation of the UTSL on a ZnO support, we simultaneously applied time-resolved *in situ* GIWAXS and GISAXS measurements to decode the growth process of the UTSLs during the sputter deposition, as illustrated by Fig. 2. ZnO supports on Si substrates were placed directly below the Ag target in a HiPIMS sputter chamber. During the Ag sputter deposition process, the incident X-ray beam impinges onto the sample with a very low incident angle, and the scattered signals are recorded by a 2D GIWAXS detector with a short SDD and a 2D GISAXS detector with a long SDD simultaneously. The time resolutions of GIWAXS and GISAXS recording were 0.5 and 0.05 s, respectively, yielding 2 and 20 2D GIWAXS and 2D GISAXS data per second. More details about the sputter deposition and the *in situ* X-ray scattering measurements are provided in the Experimental section and Fig. S5 (ESI†).

We investigated the crystalline structure evolution of sputter-deposited Ag layers on ZnO supports without and with Au surfactant based on the *in situ* GIWAXS data. As shown in Fig. 3(a) and (b), the evolution of the *in situ* GIWAXS data as a function of the effective Ag thickness provides crystalline information of the sputter-deposited Ag and ZnO support (Au surfactant). Data were plotted as azimuthally integrated line profiles of the 2D GIWAXS data (selected raw data are shown in Fig. S6, ESI†) recorded during the Ag sputter processes. With ongoing Ag sputter deposition, the Ag (111) and Ag (200) peaks of the face-centered cubic (fcc) structure formed on both supports at q = 2.6 Å and q = 3.0 Å, respectively.[62,63] As indicated by the dashed lines in Fig. 3(a) and (b), on the ZnO support with Au surfactant, the formation of crystallized Ag clusters (at $\delta_{Ag} \approx$ 0.8 nm) appeared earlier than that (at $\delta_{Ag} \approx$ 1.8 nm) on the bare ZnO support. The signals from both ZnO supports were also recorded in a broad region of $q \approx$ 2.1–2.4 Å. Compared with the scenario on the bare ZnO support, the ZnO support with Au

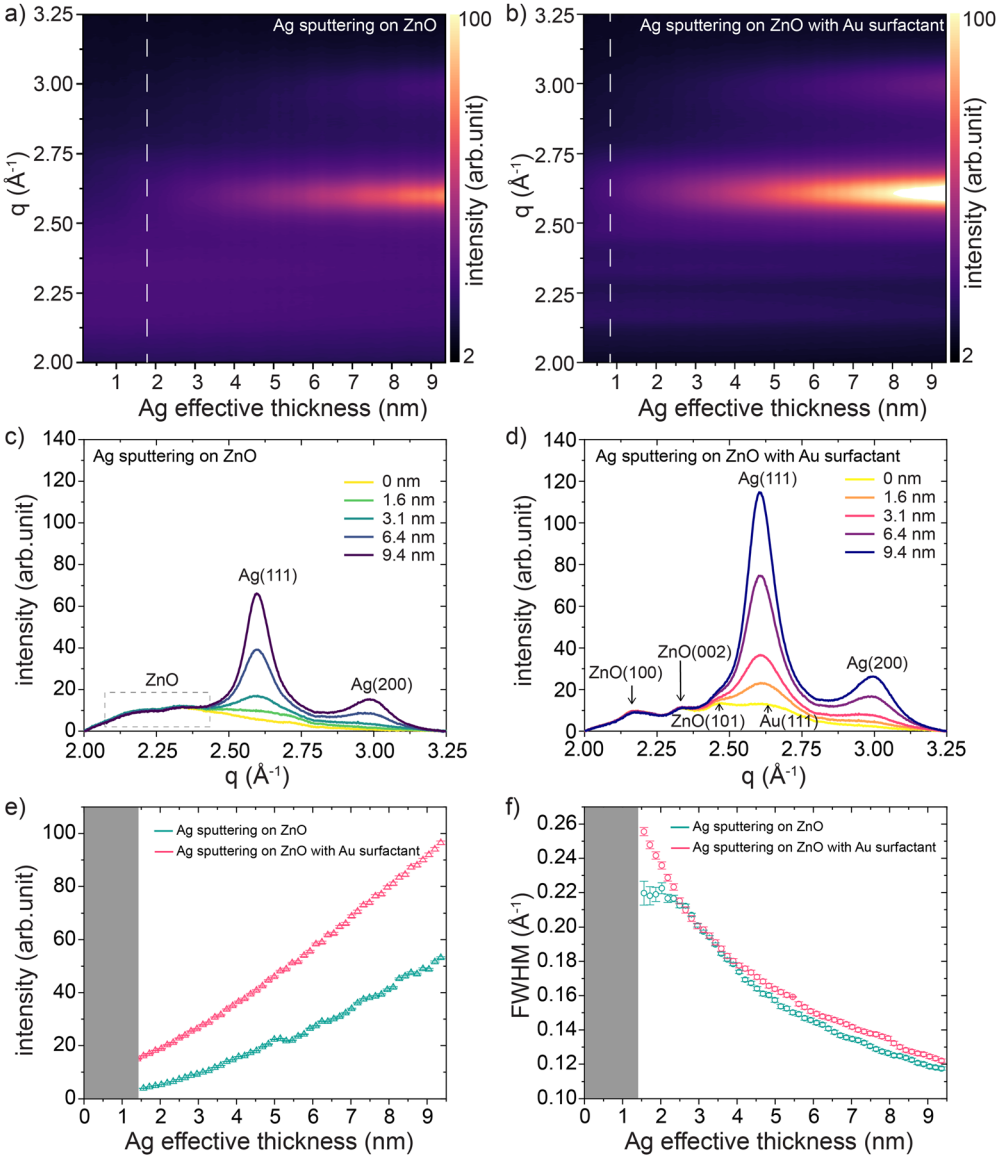

Fig. 3 Evolution of *in situ* GIWAXS data plotted as azimuthally integrated line profiles of the 2D GIWAXS data as a function of δ_{Ag} during the HiPIMS Ag sputter deposition processes on (a) the bare ZnO support and (b) the ZnO support with Au surfactant. Selected azimuthal integrations of the 2D GIWAXS data for the Ag sputter processes on (c) the bare ZnO support and (d) the ZnO support with Au surfactant at different δ_{Ag}. Evolutions of fitted (e) intensities and (f) FWHM values of the Ag (111) peak as a function of δ_{Ag} during the Ag sputter processes on the bare ZnO support and the ZnO support with Au surfactant. The gray areas refer to the resolution of extracting the intensities and FWHM values of the Ag (111) peaks.

surfactant showed ZnO-related peaks with a better degree of separation, which was attributed to the increased contrast in the presence of the Au nanoparticles. For a clearer presentation, we separately plotted several azimuthal integration lines of 2D GIWAXS data for the Ag sputter processes on both supports at selected Ag effective thicknesses, as shown in Fig. 3(c) and (d). In Fig. 3(d), the ZnO-related peaks can be clearly distinguished as ZnO (100), ZnO (002), and ZnO (101) peaks,[64,65] whereas the corresponding signals (indicated by the dashed-line box) in the same region in Fig. 3(c) are hardly distinguishable from each other. This observation is also evidence that the pre-deposited Au nanoparticles enhanced the contrast in the GIWAXS signal. The signal of the Au (111) peak from the pre-deposited Au surfactant was also detected before the start of the Ag sputter deposition. Due to the quite close position of the Au (111) and Ag (111) peaks, the signal of the Au (111) peak was obscured by the increased signal of the Ag (111) peak with ongoing Ag deposition. We applied Gaussian functions to fit the azimuthal line profiles of the 2D GIWAXS data for both sample types, obtaining the intensity and evolutions of the Ag (111) peaks, as shown in Fig. 3(e) and (f), respectively. During the sputtering process, the intensities of the Ag (111) peaks from both ZnO supports exhibited an increasing trend, indicating the formation of crystallized Ag clusters and an increase in the crystallinity of the Ag clusters. As shown in Fig. 3(e), the intensities of the Ag (111) peak during

Ag HiPIMS sputter deposition on the ZnO support with Au surfactant were higher than those during Ag sputtering on the bare ZnO support, meaning that the crystallinity of the formed Ag clusters was higher. The full width at half maximum (FWHM) values of the Ag (111) peaks of the formed Ag crystals on both ZnO supports exhibited a similar decreasing trend with increasing effective Ag thicknesses, referring to the increased crystallite size of the Ag clusters during the sputter deposition processes as extracted from the Scherrer equation.[66] In the latter part of the sputter deposition process ($\delta_{Ag} > 4$ nm), the FWHM values of the Ag (111) peak on the bare ZnO support started to become slightly lower than during the Ag sputtering on the ZnO support with Au surfactant, indicating the slightly larger size of the Ag crystals.

The morphology evolution of HiPIMS sputter-deposited Ag clusters is pivotal in understanding the UTSL formation process and how the Au surfactant could affect the formation. Therefore, we focused on decoding the morphology evolution during the formation processes of sputter-deposited UTSLs on both the bare ZnO support and the ZnO support with Au surfactant, based on the analysis of the *in situ* GISAXS data. The overviews of the UTSL formation processes on both ZnO supports are presented by contour plots of the horizontal line cuts of the *in situ* 2D GISAXS data recorded during the Ag sputter deposition processes (selected raw data are shown in Fig. S7, ESI†), as shown in Fig. 4(a) and (b). For both cases, the similar low q_y-direction-shift trends of the Ag cluster peaks (as indicated by the white arrows) refer to the reduction of the distances between the deposited Ag clusters due to the continuous coalescence and growth of the Ag clusters. In Fig. 4(a), an initial stage ($\delta_{Ag} \leq 0.9$ nm, as indicated by the white dash line) for the nucleation and Ag cluster formation can be recognized.

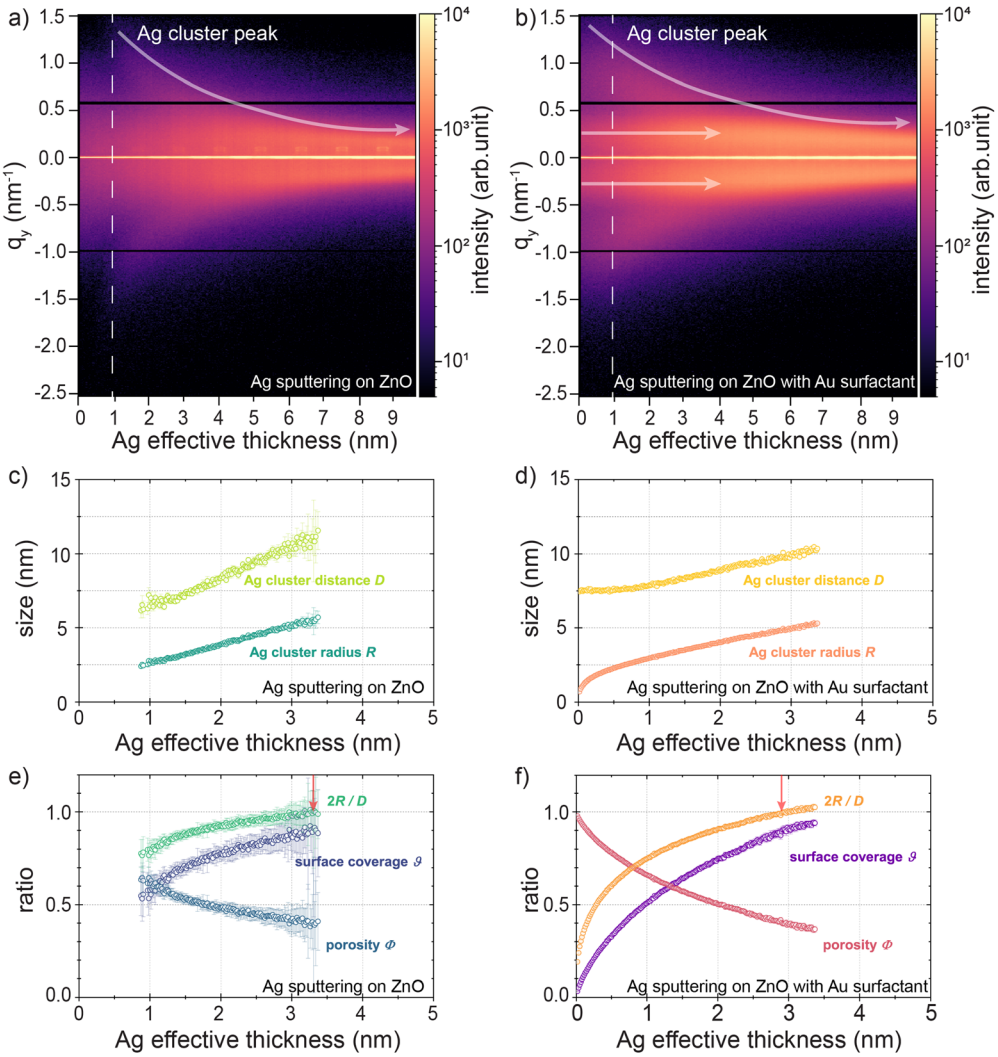

Fig. 4 Mapping of the horizontal line cuts of the *in situ* 2D GISAXS data as a function of δ_{Ag} during the HiPIMS Ag sputter deposition on (a) the bare ZnO support and (b) the ZnO support with Au surfactant. The evolution of average real space parameters as a function of the δ_{Ag}: radius of the Ag cluster R and the correlation distance between Ag clusters D, for Ag sputter deposition on (c) the bare ZnO support and (d) the ZnO support with Au surfactant. The evolution of morphological parameters as a function of the δ_{Ag}: Ag cluster diameter to distance ratio $2R/D$, Ag layer surface coverage θ, and Ag layer porosity Φ, for Ag sputter deposition on (e) the bare ZnO support and (f) the ZnO support with Au surfactant.

This initial stage initially formed nuclei and tiny clusters with sizes beyond the resolution limit of the GISAXS detection range. In contrast, Fig. 4(b) shows a pair of peaks located symmetrically at $q_y \approx \pm 0.2$ nm^{-1}, and the second-order peaks at higher q_y values could be detected from the very beginning of the Ag sputter deposition. This signal originates mainly from the contribution of pre-deposited Au nanoparticles. Compared to the Ag atoms that were just deposited on the ZnO surface, the pre-deposited Au nanoparticles were large enough to contribute a scattering signal in the current GISAXS geometry. With ongoing Ag sputtering, the symmetrical peaks remained at constant positions until $\delta_{Ag} \approx 4$ nm with increasing peak intensity. This behavior indicates that the pre-deposited Au nanoparticles play the role of a template for Ag growth. In the beginning and early stages of the Ag sputtering, parts of the Ag atoms and small clusters accumulated around the Au nanoparticles with a relatively stable inter-distance, corresponding to the constant peak position and increased peak intensity, which will be discussed later. The peaks were still visible at the end of the Ag sputtering ($\delta_{Ag} \approx 9.4$ nm) but slightly shifted towards lower q_y values, indicating that the template effect became weaker with increasing the Ag loading. Large Ag clusters gradually dominated the signal contribution in the later stage of the Ag sputtering. These changes in the peak position and intensity can be seen in the plot of the horizontal line cuts of the 2D GISASX data, as shown in Fig. S8(b) (ESI†).

To quantitatively determine the morphology evolution of sputter-deposited UTSLs on both substrates, the bare ZnO support and the ZnO support with Au surfactant, we applied a geometrical model to extract several average real-space parameters related to the growth behavior of UTSLs from the *in situ* GISAXS data. This geometrical model assumes that the sputter-deposited metal clusters are hemispherical with a radius R and are distributed in a local hexagonal arrangement with a correlation distance D. The determination of the correlation distance D can be based on the relation $D \approx 2\pi\, {q_i}^{-1}$, where q_i signifies the fitted position value of Ag cluster peak derived from the horizontal line cuts of the *in situ* GISAXS data. Fits were accomplished by using a linear combination of the Lorentzian and Gaussian functions. Regarding the average radius R, the determination was realized by an equal volume assumption. A detailed description of the geometrical model can be found in Fig. S9 (ESI†) (and the corresponding description), and also in previous publications.[49,67] Fig. 4(c) and (d) present the evolution of the average radius R and the correlation distance D for the sputter-deposited Ag clusters on bare ZnO and ZnO with Au surfactant supports, respectively. It should be noted that we only fit a part of the horizontal line cuts of the *in situ* GISAXS data within the $\delta_{Ag} \leq 3.4$ nm range of the sputter deposition processes because the contrast of the Ag cluster peaks decreased fast with increasing δ_{Ag} so that it was no longer distinguishable in the fits. For the Ag sputter deposition on the bare ZnO support, the fit process started from $\delta_{Ag} = 0.9$ nm due to the resolution limitation as mentioned above. Specifically, the average radius R of sputter-deposited Ag clusters on the bare ZnO support increased from 2.4 ± 0.1 nm to 5.7 ± 0.4 nm when the δ_{Ag} increased from 0.9 nm to 3.4 nm; meanwhile, the correlation distance D increased from 6.2 ± 0.5 nm to 11.5 ± 1.3 nm. In comparison, when sputtering Ag on ZnO with Au surfactant support, the average radius R of sputter-deposited Ag clusters increased from 0.9 ± 0.1 nm to 5.3 ± 0.1 nm when the δ_{Ag} increased from 0 nm to 3.4 nm; at the same time, the correlation distance D increased from 7.5 ± 0.1 nm to 10.4 ± 0.1 nm. Notably, as presented in Fig. 4(d), in the initial stage of Ag sputter deposition on the ZnO support with Au surfactant ($\delta_{Ag} \leq 0.5$ nm), the correlation distance D of Ag clusters almost stabilized at around 7.5 ± 0.1 nm while the average radius R increased from 0.9 ± 0.1 nm to 2.3 ± 0.1 nm. This can be attributed to the assumption that during the initial stage of Ag sputter deposition, the pre-deposited Au nanoparticles acted as fixed nuclei to adsorb Ag adatoms, which promoted the faster formation of Ag clusters and further formation of the UTSL. Based on the obtained average radius R and correlation distance D of sputter-deposited Ag clusters, we further calculated several morphological parameters during the Ag sputter deposition on both, the bare ZnO support and the ZnO support with Au surfactant, including the Ag cluster diameter to distance ratio $2R/D$, the Ag layer surface coverage θ, and the Ag layer porosity Φ. The evolution of these morphological parameters with the increasing values of δ_{Ag} during the Ag sputter deposition on both the bare ZnO support and ZnO support with Au surfactant are presented in Fig. 4(e) and (f), respectively. For both cases, the diameter-to-distance ratios $2R/D$ of Ag clusters increased during the sputter deposition processes due to the continuous growth of sputter-deposited Ag clusters. The point when $2R/D = 1$ is regarded as an important indicator when most of the deposited Au clusters interconnect with each other and form compact regions at local areas, which is the so-called percolation threshold. The percolation threshold theoretically refers to when sputter-deposited Ag clusters form a UTSL with mostly continuous morphology. We observed that the percolation threshold of the UTSL formed by Ag sputter deposition on the ZnO support with Au surfactant was reached at a lower thickness of $\delta_{Ag} = 2.9 \pm 0.1$ nm when compared to that without Au surfactant ($\delta_{Ag} = 3.3 \pm 0.1$ nm). Correspondingly, the surface coverage θ increased during both sputter processes because of the Ag accumulation and the porosities of Ag layers decreased inversely, following both the general trend of faster changes due to the presence of the Au surfactant layer. It should be noted here that the percolation thresholds of UTSLs extracted from the *in situ* GISASX data are theoretical values based on the geometric model mentioned above. Due to the assumption of a homogeneous distribution of Ag clusters, these values should slightly underestimate percolation. Additionally, compared with the data in Fig. 4(d) and (f), the fitted and further calculated data in Fig. 4(c) and (e) have larger error bars. This is attributed to the lower GISAXS signal contrast in the case of Ag sputter deposition on the bare ZnO support, which was also found in the GIWAXS data.

Based on such an analysis, we proposed a possible mechanism to elucidate the effect of the Au surfactant on the formation of the UTSL on the ZnO support, which suggests

that the pre-deposited Au nanoparticles act as nuclei or growth cores for the formation of fixed Ag clusters. This effect can lead to the formation of a continuous and smooth UTSL prepared by HiPIMS with less Ag loading. Fig. 5 schematically illustrates (based on a local perspective) the growth processes of UTSLs on both types of investigated ZnO supports and highlights the differences between them. As shown in Fig. 5(a), on the bare ZnO support, sputter-deposited Ag normally follows a typical 3D growth mode with four stages, following typical metal growth as seen before with *in situ* GISAXS analysis.[21] At the very beginning of the Ag sputter deposition, sputtered Ag atoms were deposited on the surface of the ZnO support and then nucleated and further grew into small clusters. This stage is defined as nucleation and cluster formation, in which formed Ag clusters start to enrich the GISAXS scattering signal at high q_y values. The newly formed small Ag clusters have a high surface energy and high mobility, leading to the growth of larger Ag clusters dominated by a continuous diffusion-mediated coalescence. With the growth of Ag clusters, their mobility and coalescence are significantly limited. Therefore, in the following stage, the growth of the Ag cluster is mainly derived from the adsorption of Ag atoms. After approaching the percolation threshold, the growth of Ag clusters is laterally restricted and then the further growth is mainly dominated by the accumulation of sputtered Ag along the vertical direction. In contrast, in the case of the sputtered Ag deposition on the ZnO support with Au surfactant, the Au surfactant-assisted accelerated growth mode of Ag is illustrated in Fig. 5(b). According to our assumption, the pre-deposited Au nanoparticles act as nuclei or growth cores that can adsorb sputtered Ag atoms, resulting in the fast formation of large and fixed Ag clusters. This is mainly attributed to the lower adsorption energy of Ag to Au compared to that of Ag to ZnO. In the areas without Au nanoparticle coverage, sputtered Ag atoms still undergo the nucleation and small cluster formation process by themselves. Thus, the existence of pre-deposited Au nanoparticles causes a

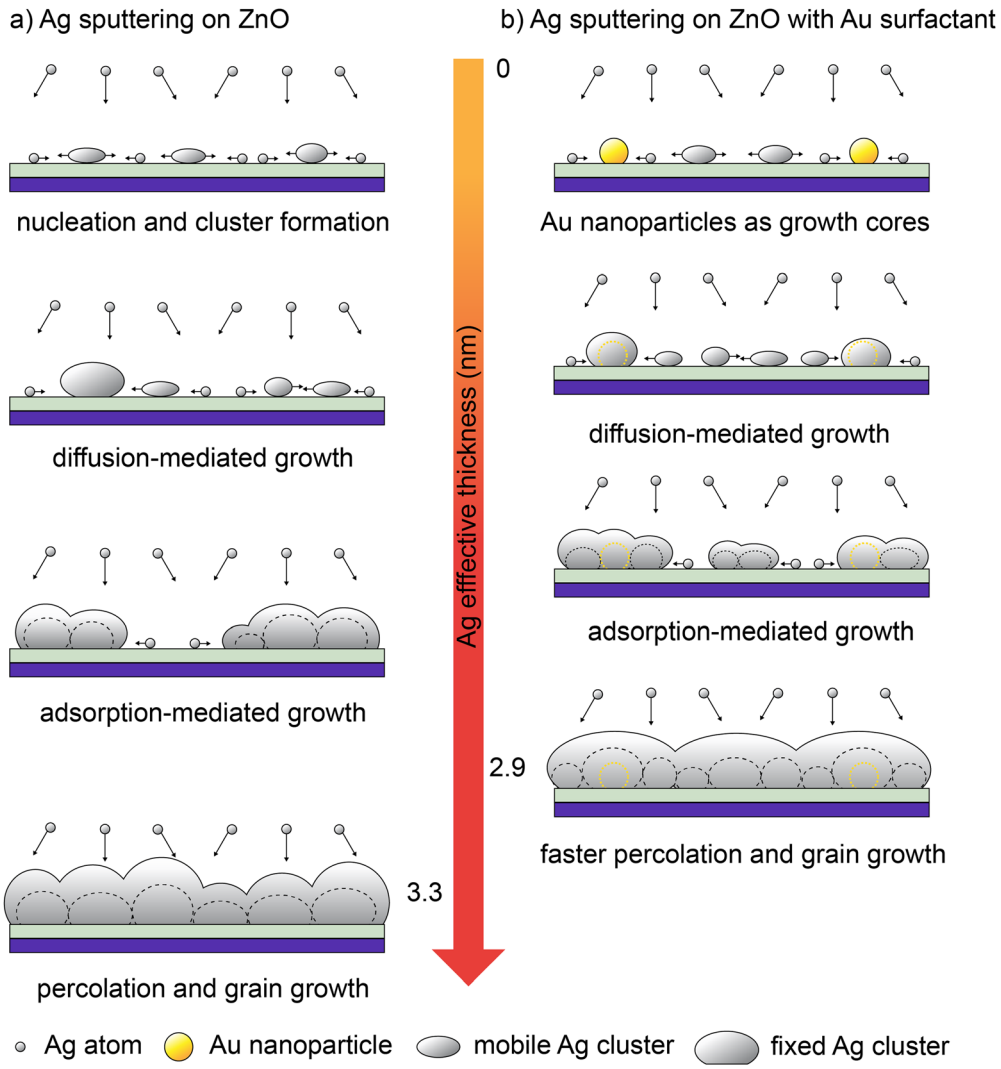

Fig. 5 Schematically localized growth processes of UTSLs (up to the percolation threshold) created *via* the HiPIMS sputter deposition of Ag on (a) the bare ZnO support and (b) the ZnO support with Au surfactant, illustrating how the Au surfactant facilitates the growth of UTSL on a ZnO support.

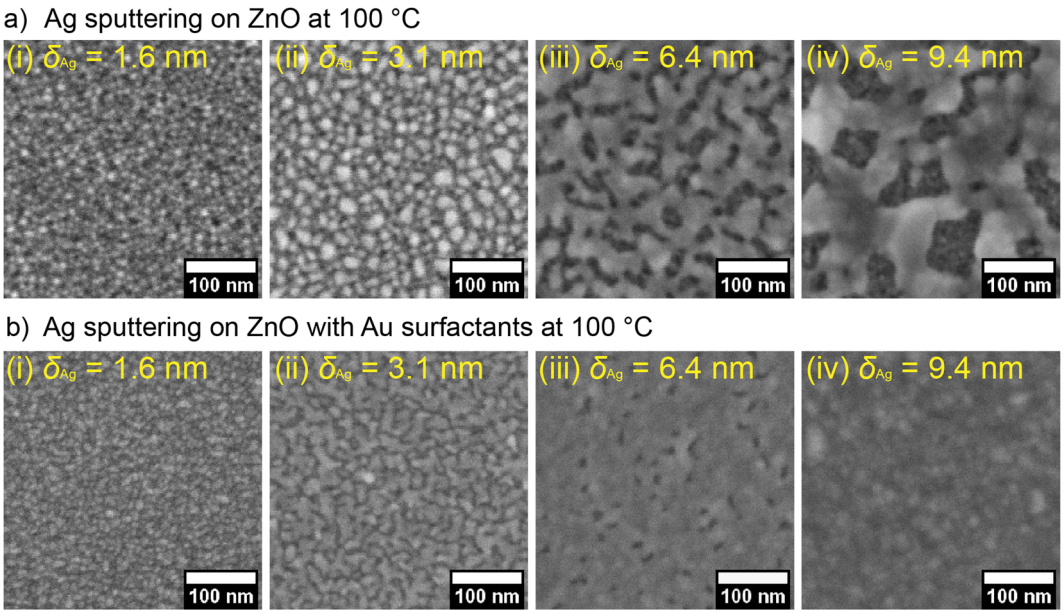

Fig. 6 FESEM images of sputter-deposited UTSLs at 100 °C on (a) the bare ZnO support and (b) the ZnO support with Au surfactant at different thicknesses of the UTSL δ_{Ag} = 1.6, 3.1, 6.4, and 9.4 nm, respectively.

part of the sputtered Ag atoms to skip the stage of nucleation and small cluster formation. After the formation of fixed Ag clusters around the Au nanoparticles, the further growth of sputtered Ag was similar to the case without Au surfactant, with the subsequent stages of diffusion-mediated coalescence, adsorption-mediated growth, and finally reaching percolation. From an overview perspective, the pre-deposited Au nanoparticles can be regarded as anchor points on the surface of the ZnO support, which can shorten the distances of Ag clusters to approach the percolation in local areas and therefore secure the formation of a continuous UTSL. The existence of a pre-deposited Au surfactant leads to a more uniform distribution of formed Ag clusters compared to the case without Au surfactant, resulting in a thinner Ag layer (a reduction of the real average thickness as shown in Fig. S1, ESI†). This finding also agrees with results from cross-sectional FESEM images. On the other hand, the increased effective thickness of the whole metallic layer due to the pre-deposited Au nanoparticles should be considered, which also contributes to the reduction of both the roughness and real average thickness.

To further demonstrate the positive effect of the pre-deposited Au surfactant on forming continuous UTSLs, we also prepared a series of UTSLs on ZnO and ZnO/Au supports, respectively, by using HiPIMS at a substrate temperature of 100 °C and with all other parameters being unchanged. FESEM images of these UTSLs prepared at 100 °C are presented in Fig. 6. Generally, high temperature negatively affects the formation of a continuous metal layer during sputter deposition due to the higher energy of the substrate induced by the thermal effect. This behavior is seen in the comparison of Fig. 1(c) and 6(a). On the bare ZnO support, the deposited UTSL at ambient temperature covered almost all areas of the ZnO underneath at δ_{Ag} = 9.4 nm (Fig. 1c-v), while the USTL deposited at 100 °C still exhibited a large part of the voids at the same effective thickness (Fig. 6a-iv). However, with the assistance of the pre-deposited Au surfactant, even at 100 °C the deposited Ag could still form an almost continuous layer at δ_{Ag} = 6.4 nm, as shown in Fig. 6(b-iii). Therefore, the positive effect of the Au surfactant on the formation of a continuous UTSL was also found at higher temperatures.

Conclusions

With HiPIMS, we prepared ULSTs on both a bare ZnO support and a ZnO support with an Au surfactant or seed layer. As already seen with FESEM images, the existence of the Au surfactant (*i.e.* the pre-deposited Au nanoparticles) or seed layer on a ZnO support has a huge effect on the growth behavior despite using HiPIMS, which as a method itself provides nucleation sites. In more detail, HiPIMS in combination with the pre-deposited Au layer led to the formation of the UTSL with a continuous morphology at a lower effective Ag thickness δ_{Ag} than that without Au surfactant. The as-prepared Ag/Au/ZnO (δ_{Ag} = 9.4 nm) thin film exhibited a higher conductivity than that of the Ag/ZnO (δ_{Ag} = 9.4 nm) thin film. Based on *in situ* GIWAXS and GISASX measurements, the effects of the Au surfactant on the formation of HiPIMS sputter-deposited UTSLs on ZnO supports were decoded. According to the *in situ* GIWAXS data, Ag crystals with Ag (100) and Ag (200) fcc structures were formed on both types of ZnO supports, irrespective of the Au surfactant. However, the existence of the Au surfactant gave rise to Ag crystals with better crystallinity. By extracting the FWHM values of the Ag (111) peaks, the similar decreasing trends of the FWHM values during both Ag sputter deposition processes indicated the continuous size growth of the Ag crystals. In the case of $\delta_{Ag} > 4$ nm, the slightly lower FWHM values of the Ag (111) peaks indicate the slightly

larger size of Ag crystals when the Au surfactant is present. The detailed morphology evolution of the sputter-deposited Ag clusters on both ZnO supports was revealed by *in situ* GISAXS measurements. For the growth of HiPIMS sputter-deposited Ag clusters, the Au surfactant enabled the theoretical percolation threshold to be reached faster at a lower effective Ag thickness of δ_{Ag} = 2.9 ± 0.1 nm compared to δ_{Ag} = 3.3 ± 0.1 nm on the bare ZnO support.

In summary, we have demonstrated that HiPIMS, a technique for the fast formation of ultra-thin metal layers, can be further improved by using pre-deposited metallic surfactant or seed layers. In this work, the pre-deposited Au surfactant (nanoparticles) can act as the nuclei or growth cores for sputtered Ag atoms, leading to the formation of large and fixed Ag clusters and finally, a continuous and smooth UTSL formation by the HiPIMS process. Even at a temperature of 100 °C, the pre-deposited Au surfactant still presented a positive effect and led to the formation of an almost continuous UTSL at δ_{Ag} = 6.4 nm. The outcomes of this work could inspire the tailoring of the morphology of sputter-deposited UTSLs in cases with or without Au surfactant, which is significant for the applications of TCEs in various electronic devices.

Author contributions

S. Liang and T. Guan contribute equally to this work. S. Liang: writing – original draft, visualization, methodology, investigation, data curation, conceptualization. T. Guan: writing – review & editing, methodology, investigation, data curation. S. Yin: writing – review & editing, methodology. S. Tu: writing – review & editing, methodology. R. Guo: writing – review & editing, methodology. Y. Bulut: writing – review & editing, methodology, investigation. K. A. Reck: writing – review & editing, methodology, investigation, instrument. J. Drewes: writing – review & editing, instrument. W. Chen: writing – review & editing, data curation. T. Strunskus: writing – review & editing, instrument. M. Schwartzkopf: writing – review & editing, methodology, data curation. F. Faupel, writing – review & editing, funding acquisition, supervision, resources. S. V. Roth: writing – review & editing, funding acquisition, supervision, resources. Y.-J. Cheng: writing – review & editing, funding acquisition, supervision. P. Müller-Buschbaum: writing – review & editing, supervision, project administration, funding acquisition, resources, conceptualization.

Data availability

All data generated or analyzed during this study are included in the published article and its ESI† and source data files. The data can also be found at the following public repository: https://mediatum.ub.tum.de/1751170.

Conflicts of interest

There are no conflicts to declare.

Acknowledgements

This work is supported by Deutsche Forschungsgemeinschaft (DFG) with funding *via* projects RO 4638/XX, FA 234/XX and MU 1487/39-1. S. L., T. G., T. Z., S. Y., S. T., R. G. acknowledge the financial support from the China Scholarship Council (CSC). W. C. acknowledges the funding support from the National Natural Science Foundation of China (No. 12204318), Guangdong Basic and Applied Basic Research Foundation (No. 2021A1515110535), and Shenzhen Science and Technology Program (Grant No. RCYX20221008092908030, ZDSYS20200811143600001). Y.-J.C. acknowledges the financial support from the National Natural Science Foundation of China (52061135110). The *in situ* X-ray scattering experiments in combination with sputter deposition were performed at the third-generation synchrotron source PETRA III at DESY in Hamburg, Germany, a member of the Helmholtz Association (HGF).

References

1 P. S. Schulze, L. A. Barreira, H. G. Pereira, J. A. Perales and J. C. Varela, *Trends Biotechnol.*, 2014, **32**, 422–430.
2 S. T. Han, H. Peng, Q. Sun, S. Venkatesh, K. S. Chung, S. C. Lau, Y. Zhou and V. Roy, *Adv. Mater.*, 2017, **29**, 1700375.
3 J. S. Park, S. Kim, Z. Xie and A. Walsh, *Nat. Rev. Mater.*, 2018, **3**, 194–210.
4 Z. L. Wang, J. Chen and L. Lin, *Energy Environ. Sci.*, 2015, **8**, 2250–2282.
5 W. Cao, J. Li, H. Chen and J. Xue, *J. Photonics Energy*, 2014, **4**, 040990.
6 Z. L. Wang, *ACS Nano*, 2013, **7**, 9533–9557.
7 H. B. Lee, W.-Y. Jin, M. M. Ovhal, N. Kumar and J.-W. Kang, *J. Mater. Chem. C*, 2019, **7**, 1087–1110.
8 C. J. Zhang and V. Nicolosi, *Energy Storage Mater.*, 2019, **16**, 102–125.
9 M. Betker, C. Harder, E. Erbes, J. E. Heger, A. E. Alexakis, B. Sochor, Q. Chen, M. Schwartzkopf, V. Körstgens and P. Müller-Buschbaum, *ACS Appl. Nano Mater.*, 2023, **6**, 13677–13688.
10 U. Betz, M. K. Olsson, J. Marthy, M. Escolá and F. Atamny, *Surf. Coat. Technol.*, 2006, **200**, 5751–5759.
11 S. Ye, A. R. Rathmell, Z. Chen, I. E. Stewart and B. J. Wiley, *Adv. Mater.*, 2014, **26**, 6670–6687.
12 W. Guo, Z. Xu, F. Zhang, S. Xie, H. Xu and X. Y. Liu, *Adv. Funct. Mater.*, 2016, **26**, 8855–8884.
13 P. Wang, M. Hu, H. Wang, Z. Chen, Y. Feng, J. Wang, W. Ling and Y. Huang, *Adv. Sci.*, 2020, **7**, 2001116.
14 O. Inganäs, *Nat. Photonics*, 2011, **5**, 201–202.
15 Y. G. Bi, Y. F. Liu, X. L. Zhang, D. Yin, W. Q. Wang, J. Feng and H. B. Sun, *Adv. Opt. Mater.*, 2019, **7**, 1800778.
16 J. Yun, *Adv. Funct. Mater.*, 2017, **27**, 1606641.
17 S. Liang, M. Schwartzkopf, S. V. Roth and P. Müller-Buschbaum, *Nanoscale Adv.*, 2022, **4**, 2533–2560.
18 D. Gaspar, A. Pimentel, T. Mateus, J. Leitão, J. Soares, B. Falcão, A. Araújo, A. Vicente, S. Filonovich and H. Águas, *Sci. Rep.*, 2013, **3**, 1469.

19 K. A. Lozovoy, A. G. Korotaev, A. P. Kokhanenko, V. V. Dirko and A. V. Voitsekhovskii, *Surf. Coat. Technol.*, 2020, **384**, 125289.
20 V. M. Kaganer, B. Jenichen, R. Shayduk, W. Braun and H. Riechert, *Phys. Rev. Lett.*, 2009, **102**, 016103.
21 M. Schwartzkopf, A. Hinz, O. Polonskyi, T. Strunskus, F. C. Löhrer, V. Körstgens, P. Müller-Buschbaum, F. Faupel and S. V. Roth, *ACS Appl. Mater. Interfaces*, 2017, **9**, 5629–5637.
22 K. Bromann, H. Brune, H. Röder and K. Kern, *Phys. Rev. Lett.*, 1995, **75**, 677.
23 G. Rosenfeld, R. Servaty, C. Teichert, B. Poelsema and G. Comsa, *Phys. Rev. Lett.*, 1993, **71**, 895.
24 C. Zhang, D. Zhao, D. Gu, H. Kim, T. Ling, Y. K. R. Wu and L. J. Guo, *Adv. Mater.*, 2014, **26**, 5696–5701.
25 L. V. Koplitz, O. Dulub and U. Diebold, *J. Phys. Chem. B*, 2003, **107**, 10583–10590.
26 S. Schubert, M. Hermenau, J. Meiss, L. Müller-Meskamp and K. Leo, *Adv. Funct. Mater.*, 2012, **22**, 4993–4999.
27 Y. Yang, Q. Chen, Y.-T. Hsieh, T.-B. Song, N. D. Marco, H. Zhou and Y. Yang, *ACS Nano*, 2015, **9**, 7714–7721.
28 B. Pattier, J.-F. Bardeau, M. Edely, A. Gibaud and N. Delorme, *Langmuir*, 2008, **24**, 821–825.
29 Y. Wu, C. Zhang, N. M. Estakhri, Y. Zhao, J. Kim, M. Zhang, X. X. Liu, G. K. Pribil, A. Alù and C. K. Shih, *Adv. Mater.*, 2014, **26**, 6106–6110.
30 R. A. Maniyara, D. Rodrigo, R. Yu, J. Canet-Ferrer, D. S. Ghosh, R. Yongsunthon, D. E. Baker, A. Rezikyan, F. J. García de Abajo and V. Pruneri, *Nat. Photonics*, 2019, **13**, 328–333.
31 S. Jiang, L. Chang, J. Luo, J. Zhang, X. Liu, C.-Y. Lee and W. Zhang, *Analyst*, 2021, **146**, 6170–6177.
32 S. D. Yambem, K.-S. Liao and S. A. Curran, *Sol. Energy Mater. Sol. Cells*, 2011, **95**, 3060–3064.
33 H. Lee and C. Lee, *Adv. Energy Mater.*, 2018, **8**, 1702197.
34 D. Zhao, C. Zhang, H. Kim and L. J. Guo, *Adv. Energy Mater.*, 2015, **5**, 1500768.
35 T. Schwab, S. Schubert, L. Müller-Meskamp, K. Leo and M. C. Gather, *Adv. Opt. Mater.*, 2013, **1**, 921–925.
36 T. Schwab, S. Schubert, S. Hofmann, M. Fröbel, C. Fuchs, M. Thomschke, L. Müller-Meskamp, K. Leo and M. C. Gather, *Adv. Opt. Mater.*, 2013, **1**, 707–713.
37 E. Jeong, G. Zhao, S. M. Yu, S.-G. Lee, J.-S. Bae, J. Park, J. Rha, G.-H. Lee and J. Yun, *Appl. Surf. Sci.*, 2020, **528**, 146989.
38 J. Huang, X. Liu, Y. Lu, Y. Zhou, J. Xu, J. Li, H. Wang, J. Fang, Y. Yang and W. Wang, *Sol. Energy Mater. Sol. Cells*, 2018, **184**, 73–81.
39 V. Logeeswaran, N. P. Kobayashi, M. S. Islam, W. Wu, P. Chaturvedi, N. X. Fang, S. Y. Wang and R. S. Williams, *Nano Lett.*, 2009, **9**, 178–182.
40 L.-H. Xu, Q.-D. Ou, Y.-Q. Li, Y.-B. Zhang, X.-D. Zhao, H.-Y. Xiang, J.-D. Chen, L. Zhou, S.-T. Lee and J.-X. Tang, *ACS Nano*, 2016, **10**, 1625–1632.
41 P. Müller-Buschbaum, *Adv. Mater.*, 2014, **26**, 7692–7709.
42 P. Müller-Buschbaum, *Anal. Bioanal. Chem.*, 2003, **376**, 3–10.
43 Y. Bulut, B. Sochor, C. Harder, K. A. Reck, J. Drewes, Z. Xu, X. Jiang, A. Meinhardt, A. Jeromin and M. Kohantorabi, *Nanoscale*, 2023, **15**, 15768–15774.
44 R. Guo, D. Han, W. Chen, L. Dai, K. Ji, Q. Xiong, S. Li, L. K. Reb, M. A. Scheel, S. Pratap, N. Li, S. Yin, T. Xiao, S. Liang, A. L. Oechsle, C. L. Weindl, M. Schwartzkopf, H. Ebert, P. Gao, K. Wang, M. Yuan, N. C. Greenham, S. D. Stranks, S. V. Roth, R. H. Friend and P. Müller-Buschbaum, *Nat. Energy*, 2021, **6**, 977–986.
45 T. Tian, S. Yin, S. Tu, C. L. Weindl, K. S. Wienhold, S. Liang, M. Schwartzkopf, S. V. Roth and P. Müller-Buschbaum, *Adv. Funct. Mater.*, 2021, **31**, 2105644.
46 S. Yin, Y. Zou, M. A. Reus, X. Jiang, S. Tu, T. Tian, R. Qi, Z. Xu, S. Liang, Y. Cheng, J. E. Heger, M. Schwartzkopf, S. V. Roth and P. Müller-Buschbaum, *Chem. Eng. J.*, 2023, **455**, 140135.
47 W. Chen, S. Liang, F. C. Löhrer, S. J. Schaper, N. Li, W. Cao, L. P. Kreuzer, H. Liu, H. Tang, V. Körstgens, M. Schwartzkopf, K. Wang, X. W. Sun, S. V. Roth and P. Müller-Buschbaum, *ACS Appl. Mater. Interfaces*, 2020, **12**, 46942–46952.
48 S. Liang, W. Chen, S. Yin, S. J. Schaper, R. Guo, J. Drewes, N. Carstens, T. Strunskus, M. Gensch, M. Schwartzkopf, F. Faupel, Y.-J. Cheng and P. Müller-Buschbaum, *ACS Appl. Mater. Interfaces*, 2021, **13**, 14728–14740.
49 S. Liang, T. Guan, S. Yin, E. Krois, W. Chen, C. R. Everett, J. Drewes, T. Strunskus, M. Gensch, J. Rubeck, C. Haisch, M. Schwartzkopf, F. Faupel, S. V. Roth, Y.-J. Cheng and P. Müller-Buschbaum, *ACS Appl. Nano Mater.*, 2022, **5**, 7492–7501.
50 R. Bandorf, S. Waschke, F. Carreri, M. Vergöhl, G. Grundmeier and G. Bräuer, *Surf. Coat. Technol.*, 2016, **290**, 77–81.
51 I.-L. Velicu, V. Tiron, C. Porosnicu, I. Burducea, N. Lupu, G. Stoian, G. Popa and D. Munteanu, *Appl. Surf. Sci.*, 2017, **424**, 397–406.
52 A. Ghailane, M. Makha, H. Larhlimi and J. Alami, *Mater. Lett.*, 2020, **280**, 128540.
53 K. A. Reck, Y. Bulut, Z. Xu, S. Liang, T. Strunskus, B. Sochor, H. Gerdes, R. Bandorf, P. Müller-Buschbaum and S. V. Roth, *Appl. Surf. Sci.*, 2024, 160392.
54 Z. Liang, T. Guan, Q. Zhang, W. Shao, J. Chen, J. Zheng, D. Li, I. Abdulhalim and L. Jiang, *Appl. Phys. Lett.*, 2019, **115**, 091604.
55 A. Buffet, A. Rothkirch, R. Döhrmann, V. Körstgens, M. M. Abul Kashem, J. Perlich, G. Herzog, M. Schwartzkopf, R. Gehrke and P. Müller-Buschbaum, *J. Synchrotron Radiat.*, 2012, **19**, 647–653.
56 D. Nečas and P. Klapetek, *Open Phys.*, 2012, **10**, 181–188.
57 Z. L. Wang, *Mater. Today*, 2004, **7**, 26–33.
58 Q. Zhang, C. S. Dandeneau, X. Zhou and G. Cao, *Adv. Mater.*, 2009, **21**, 4087–4108.
59 L. Schmidt-Mende and J. L. MacManus-Driscoll, *Mater. Today*, 2007, **10**, 40–48.
60 C. T. Campbell, *Surf. Sci. Rep.*, 1997, **27**, 1–111.
61 V. Tolmachev, Y. A. Zharova and S. Grudinkin, *Opt. Spectrosc.*, 2020, **128**, 2002–2007.
62 Q. Chen, C. J. Brett, A. Chumakov, M. Gensch, M. Schwartzkopf, V. Körstgens, L. D. Söderberg, A. Plech,

P. Zhang and P. Müller-Buschbaum, *ACS Appl. Nano Mater.*, 2021, **4**, 503–513.
63 Y. Zhao, N. Kornienko, Z. Liu, C. Zhu, S. Asahina, T.-R. Kuo, W. Bao, C. Xie, A. Hexemer and O. Terasaki, *J. Am. Chem. Soc.*, 2015, **137**, 2199–2202.
64 Y. H. Lee, Y. T. Hsu, P. S. Yeh, W. Y. Sun and C. W. Lee, *Phys. Status Solidi A*, 2019, **216**, 1801001.
65 M. Lučić Lavčević, P. Dubček, S. Bernstorff, M. Pavlović and L. Šilović, *J. Nanomater.*, 2013, **1**, 381519.
66 F. T. L. Muniz, M. R. Miranda, C. Morilla dos Santos and J. M. Sasaki, *Acta Crystallogr., Sect. A: Found. Adv.*, 2016, **72**, 385–390.
67 M. Schwartzkopf, A. Buffet, V. Körstgens, E. Metwalli, K. Schlage, G. Benecke, J. Perlich, M. Rawolle, A. Rothkirch and B. Heidmann, *Nanoscale*, 2013, **5**, 5053–5062.